crystals

MDPI

Article

Synthesizing Iron Oxide Nanostructures: The Polyethylenenemine (PEI) Role

Sergio Lentijo Mozo †, Efisio Zuddas †, Alberto Casu *,† and Andrea Falqui *

Biological and Environmental Sciences and Engineering (BESE) Division, Nanostructures & Biotech Laboratory (NABLA Lab), King Abdullah University of Science and Technology (KAUST), 23955-6900 Thuwal, Saudi Arabia; sergio.lentijomozo@kaust.edu.sa (S.L.M.); efisio.zuddas@kaust.edu.sa (E.Z.)

* Correspondence: alberto.casu@kaust.edu.sa (A.C.); andrea.falqui@kaust.edu.sa (A.F.); Tel.: +966-544-700060 (A.F.)

† These authors contributed equally to this work.

Academic Editor: Roberto Comparelli
Received: 23 November 2016; Accepted: 9 January 2017; Published: 12 January 2017

Abstract: Controlled synthesis of anisotropic iron oxide nanoparticles is a challenge in the field of nanomaterial research that requires an extreme attention to detail. In particular, following up a previous work showcasing the synthesis of magnetite nanorods (NRs) using a two-step approach that made use of polyethylenenemine (PEI) as a capping ligand to synthesize intermediate β-FeOOH NRs, we studied the effect and influence of the capping ligand on the formation of β-FeOOH NRs. By comparing the results reported in the literature with those we obtained from syntheses performed (1) in the absence of PEI or (2) by using PEIs with different molecular weight, we showed how the choice of different PEIs determines the aspect ratio and the structural stability of the β-FeOOH NRs and how this affects the final products. For this purpose, a combination of XRD, HRTEM, and direct current superconducting quantum interference device (DC SQUID) magnetometry was used to identify the phases formed in the final products and study their morphostructural features and related magnetic behavior.

Keywords: magnetic nanoparticles; akaganeite; magnetite; hematite; polyethylenenemine; superparamagnetic behavior

1. Introduction

Magnetite (Fe_3O_4) magnetic nanoparticles (NPs) are still widely recognized as an interesting material, despite having been the long-lasting subject of many studies, due to their versatility in terms of application in many diverse fields, ranging from catalysis [1] and magnetic information storage [2] and extending to medical and theranostic applications such as magnetic resonance imaging (MRI) [3], drug delivery [4], and magnetic hyperthermia [5]. Consequently, diverse synthetic approaches—including coprecipitation [6], hydrothermal–solvothermal [7], sol–gel [8], and thermal decomposition [9]—have been developed to engineer NP features accordingly, always striving towards the common goal of obtaining monodisperse NPs, easily and finely tuning their size and shape in a most reproducible way.

Recently, the design and controlled fabrication of anisotropic magnetite NPs attracted much attention, since the punctual control over particle size and shape in such anisotropic systems could be the key factor in tailoring their magnetic properties over a wide range of values [10]. However, the synthesis of these anisotropic iron oxide nanocrystals is nontrivial, more so for one-dimensional (1D) systems such as nanorods (NRs), nanotubes (NTs), and nanowires (NWs), with different strategies being proposed to reach this goal [11–13]. Among them, a process involving the dehydration and/or reduction of premade elongated β-FeOOH with a channel-type nanoporous structure (akaganeite) seems particularly promising. In fact, β-FeOOH, whose natural formation is due to the corrosion of iron in chloride-containing environments, is an antiferromagnetic oxy-hydroxide material [14], usually synthesized by hydrolysis of $FeCl_3 \cdot 6H_2O$ with typical shapes of nanospindles and nanorods due to its crystallographic features [15,16]. If these shapes could be maintained during reduction, considering that in such a process the crystal defects and porosity of the structure could increase systematically, magnetite with different morphologies would be gained.

Since Chen and coworkers first reported the preparation of anisotropic iron particles by reduction of β-FeOOH particles prepared by hydrolysis of ferric chloride [17], extensive studies have been carried out to investigate the formation mechanisms and control over morphology for the synthesis of iron oxide nanoparticles via oxy-hydroxide NPs. Peng et al. were among the first to demonstrate the preparation of magnetite NRs by a hydrothermal reduction at high temperature of β-FeOOH NRs, which were firstly prepared by a typical hydrolysis process of an iron complex [18]. Later, different groups moved from this two-step approach to obtain magnetite NRs [19–21] and various other anisotropic magnetite NPs, such as hollow magnetite NRs [22]; porous, size-modulated NRs [23]; and nanoellipsoids [24].

In this framework, a very recent study by Mohapatra et al. gave further insight to the synthesis of uniform colloidal magnetite NRs by a two-step strategy. First, the authors described the synthesis of β-FeOOH NRs with different lengths and diameters by hydrolysis of $FeCl_3$ in presence of polyethylenimine (PEI) as the capping agent, showing that the length and diameter of the β-FeOOH NRs could be controlled from 70 to 25 nm and 12 to 3 nm, respectively, by increasing the PEI concentration from 0.2 mL to 2 mL. In a second step, oleylamine (OLA) was used as a reducing agent, leading to the conversion from β-FeOOH NRs to magnetite (Fe_3O_4) NRs, while retaining the original size and shape. Also, the authors reported that the final product was subjected to magnetic separation. This suggests that different iron oxide phases were probably synthesized in that second reaction step, because the purification step indicates the presence of different magnetic and nonmagnetic iron oxide phases [25]. Although this last approach seems to be very promising for synthesizing 1D anisotropic magnetite shapes, the description of the PEI capping agent was overlooked, despite its key role in the formation mechanism of β-FeOOH NRs. Due to the existence of diverse types of PEI polymers from different vendors, a thorough description should take into account other information, such as the average molecular weight and the type (branched or linear) of polymer used in the synthesis.

Since, to the best of our knowledge, no previous studies were conducted on the role of different types of PEI in the synthesis of β-FeOOH NRs, in this work we decided to follow up on the synthetic procedure of Fe_3O_4 NRs described by Mohapatra to deeply investigate the effect and influence of PEI on the formation and morphological properties of synthesized β-FeOOH NRs by keeping the same reaction conditions and only varying the PEI. Since PEI is a well-established and widely known capping agent, used to control the shape and size of many different nanosized systems [26,27], we studied and compared the different outcomes obtained by heating treatment of the β-FeOOH NPs that had been achieved by reaction processes performed (1) in the absence of PEI; (2) by addition of a low weight-average molecular weight PEI (800 g/mol); or (3) a PEI of high weight-average molecular weight (25,000 g/mol). In particular, we found that the iron oxide nanostructures obtained by a heating treatment of β-FeOOH NRs in presence of OLA cannot retain the shape and size of the starting nanorods and, moreover, the as-prepared nanostructures are constituted by two different phases (i.e., hematite and magnetite). Both phases can be detected by XRD analysis when the final nanostructures are not purified by a magnetic separation technique after their synthesis.

2. Results

2.1. Synthesis of the Materials

2.1.1. Preparation of β-FeOOH NRs

No PEI Addition

$FeCl_3 \cdot 6H_2O$ (20 mmol) was dissolved in 100 mL of deionized water and heated at 80 °C for 4 h under magnetic stirring. After that, an orange solid was precipitated and separated by centrifugation and washed several times with acetone. This sample will be called FeOOH_nopei.

PEI Addition

A solution of 0.2 mL of PEI and 50 mL of deionized water was added to a solution of 20 mmol of $FeCl_3 \cdot 6H_2O$ in 50 mL of deionized water. After that, the final solution was heated to 80 °C for 4 h under magnetic stirring. Finally, an orange solid was precipitated and separated by centrifugation and washed several times with acetone. This NP synthesis procedure was repeated twice with different types of PEI polymers: PEI with M_w = 800 g/mol and PEI with M_w = 25,000 g/mol. The two samples will be called FeOOH_800 and FeOOH_25000.

2.1.2. Reduction of β-FeOOH NRs

A mixture of 150 mg of β-FeOOH NRs and 5 g of OLA was prepared under N_2 atmosphere and heated to 200 °C for 4 h. After that, the final black mixture was cooled down at room temperature and washed with acetone several times. After washing, the NPs were dried, redissolved, and stored in hexane. This NP synthesis procedure was repeated three times with the three different samples of β-FeOOH NRs as starting material. The final three samples will be called FeO_nopei, FeO_800, and FeO_25000.

3. Characterization of the Materials by XRD, TEM, HRTEM, and SQUID Magnetometry

To characterize the morphological and structural features of the samples whose synthesis was described above (FeOOH_nopei, FeOOH_800, FeOOH_25000, FeO_nopei, FeO_800 and FeO_25000), X-ray diffraction (XRD), transmission electron microscopy (TEM), and high-resolution transmission electron microscopy (HRTEM) analyses were carried out. Superconducting quantum interference device (SQUID) magnetometry measurements were carried out to determine the magnetic behavior of the sole iron oxide specimens (FeO_nopei, FeO_800, and FeO_25000).

3.1. Characterization of β-FeOOH NRs

Figure 1a–c shows the typical diffraction patterns of the as-synthesized NRs, which correspond to the characteristic tetragonal structure of β-FeOOH, consistent with the reported values (JCPD 00-034-1266), which confirm the purity of the NRs and the absence of other crystalline structures.

In Figure 1d–f, conventional TEM images of the three starting samples (β-FeOOH NRs) are reported, respectively. The FeOOH_nopei sample features spindle-shaped NPs with a mean length l = 291 ± 35 nm and a mean diameter d = 42 ± 5 nm. The FeOOH_800 and FeOOH_25000 samples feature rod-shaped NPs with a mean length l = 32 ± 7 nm and 38 ± 7 nm, respectively, and similar mean diameter d = 5.1 ± 1.0 nm and 5.7 ± 1.0 nm.

HRTEM structural characterization was performed to confirm the formation of the akaganeite β-FeOOH crystal structure in both the NPs synthesized with and without PEI. Figure 2 displays representative HRTEM images of single β-FeOOH NPs along with the corresponding 2-dimensional fast Fourier transform (2D-FFT) patterns. Lattice sets obtained by analyzing 2D-FFT patterns are consistent with the formation of single crystal structures of akaganeite (JCPD 00-034-1266), in accordance with what was already shown by XRD.

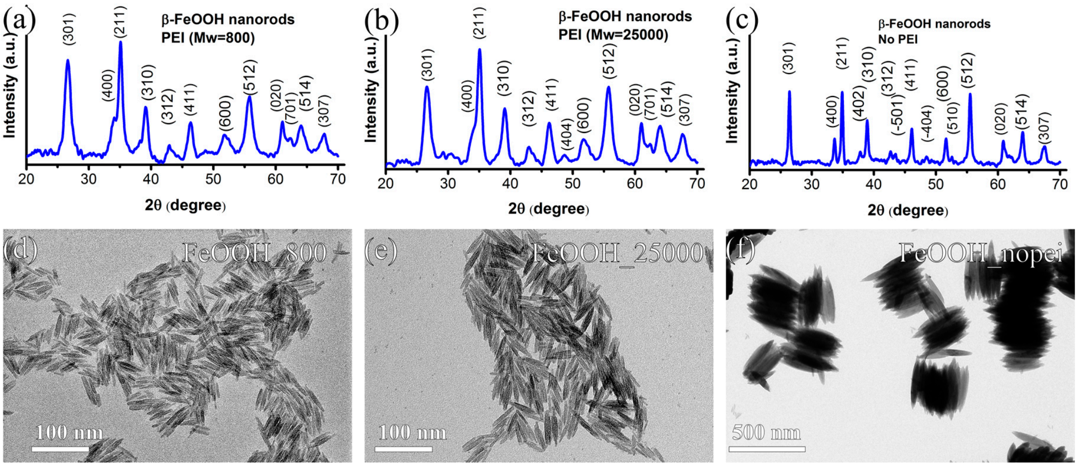

Figure 1. XRD patterns and conventional TEM images of the samples FeOOH_800 (**a**,**d**); FeOOH_25000 (**b**,**e**); and FeOOH_nopei (**c**,**f**).

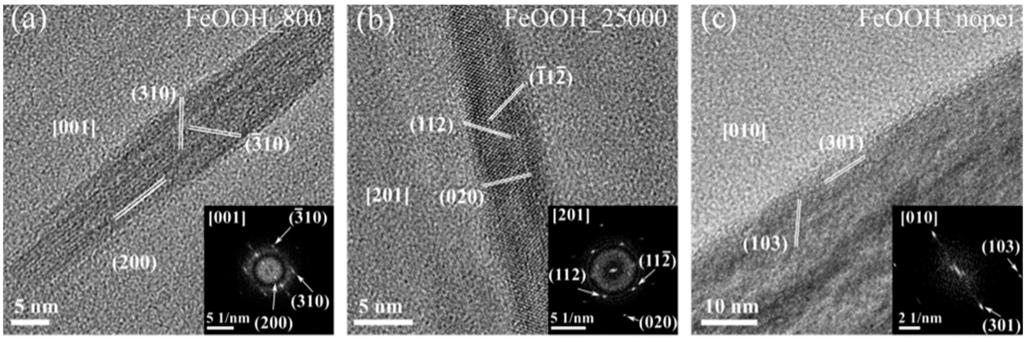

Figure 2. HRTEM images and corresponding 2-dimensional fast Fourier transform (2D-FFT) patterns of β-FeOOH nanoparticles (NPs) prepared with low M_w polyethylenimine (PEI) (**a**); with high M_w PEI (**b**); and without PEI (**c**).

3.2. Characterization of Iron Oxide Nanostructures

Figure 3a–c shows the XRD patterns of the as-prepared iron oxide nanostructures. The ones of the FeO_25000 samples and FeO_nopei (Figure 3b,c) reveal the presence of two coexisting phases, namely magnetite (Fe_3O_4) and hematite (α-Fe_2O_3). In fact, while the most intense diffraction peaks at 30.11, 35.4, 43.06, 53.3, 56.92, and 62.40 degrees are consistent with the formation of magnetite, (JCPD 00-019-0629), an additional set of less intense peaks at 33.1, 40.8, 49.41, 53.4, and 63.9 degrees also indicate the presence of hematite (JCPD 00-033-0664). The secondary hematite phase formed in the FeO_25000 sample (Figure 3b) seems to exhibit a higher degree of crystallinity with respect to the one observed in the FeO_nopei (Figure 3c), as evidenced by the presence of a higher number of narrower diffraction peaks. On the other hand, the XRD pattern of the FeO_800 sample (Figure 3a) only shows peaks corresponding to the magnetite phase, thus confirming the complete transformation of β-FeOOH phase into iron oxide phases after the reduction in all the samples.

Conventional TEM imaging of the three reduced samples (Figure 3d–f) clearly shows the effects of the reduction on the shape and size of the final NPs. In particular, the FeO_nopei sample (Figure 3f) still features spindle-shaped NPs with a mean length and diameter of $l = 212 \pm 25$ nm and $d = 46 \pm 6$ nm, which means that the size and shape of the original NPs is generally maintained, albeit with a decrease in length. However, major modifications were observed in the FeO_800 and FeO_25000 samples (Figure 3d,e) that show a mixture of nanostructures of varying shape and size (17.2 ± 4.7 nm and 21.4 ± 6.2 nm, respectively). The dramatic variation in shape and size observed in the latter samples after reduction is evident from the increased values of standard deviation and from the transition from a rodlike shape to irregular, less anisotropic shapes. This implies that size analysis cannot be conducted anymore in terms of length and diameter but just in the more generic terms of size, since the features of the starting NRs could not be retained in the reduced samples.

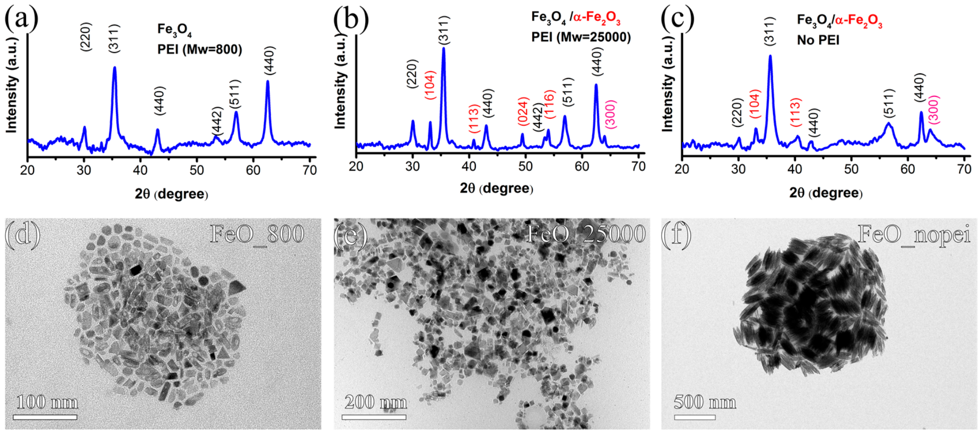

Figure 3. XRD patterns and conventional TEM images of the samples FeO_800 (**a**,**d**); FeO_25000 (**b**,**e**); FeO_nopei (**c**,**f**).

On the other hand, HRTEM provided a further insight on the structural features of the reduced samples. In particular, the structural analysis of the 2D-FFT patterns highlighted the presence of the magnetite phase in all the samples, while hematite domains were only found among the analyzed NPs of the FeO_25000 and FeO_nopei samples, as displayed in Figure 4, in agreement with what shown by the corresponding XRD patterns reported in Figure 3a–c. Moreover, an extended analysis over the different shapes and sizes observed in the reduced samples evidenced that no association could be made between these polydisperse populations and the occurrence of magnetite and hematite phases, suggesting that the formation of the secondary hematite phase cannot be associated with specific shapes of the reduced NPs.

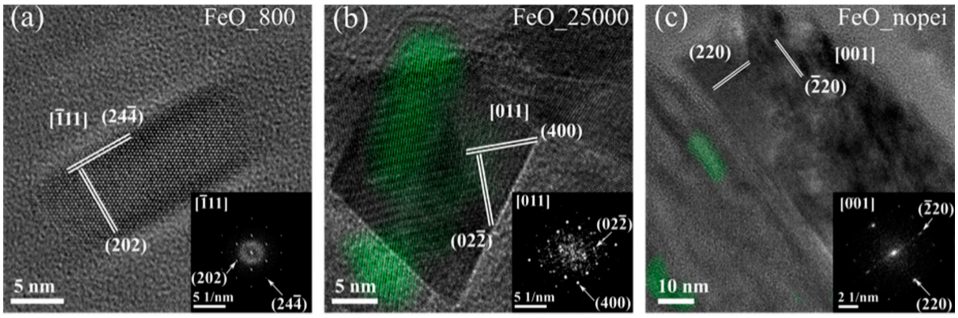

Figure 4. HRTEM images and corresponding 2D-FFTs of representative NPs from the FeO_800 (**a**); FeO_25000 (**b**); FeO_nopei (**c**) samples. Full structural characterization of the magnetite phase is provided in each inset, while the false-colored green areas in the main (**b**,**c**) panels indicate the presence of a hematite phase, as obtained by inverse 2D-FFT of its typical (104) peak (2.6996 nm).

Finally, the magnetic characterization of the reduced samples was performed in order to give a further insight on the effects of the antiferromagnetic-to-ferrimagnetic phase transition (i.e., from α-Fe_2O_3 to Fe_3O_4) of the nanostructures. Direct current (DC) magnetization was measured as a function of temperature in the low-field regime (50 Oe) in the 4–400 K range according to the zero-field-cooled/field-cooled (ZFC–FC) protocols, while isothermal hysteresis loops of the magnetically blocked samples were recorded at 4 K.

No superimposition of the ZFC and FC magnetization curves can be observed for any of the samples, which implies that the NPs are still in a blocked state at 400 K and that no superparamagnetic relaxation can be observed within the experimental thermal range (Figure 5a). However, some additional information can be obtained from the analysis of the ZFC–FC and the derivative d(ZFC–FC)/dT curves. In fact, the Verwey transition, which indicates a structural reorganization from cubic to monoclinic structure of Fe_3O_4 at low temperature, can be observed in all the samples with T_V = 115 K for the FeO_800 sample and T_V = 110 K in the other cases. While the appearance of the Verwey transition in all the ZFC–FC curves suggests the formation of highly crystalline Fe_3O_4 NPs with a low superficial disorder [28], the variation in T_V values indicates the formation of a Fe-deficient $Fe_{3\text{-}x}O_4$ phase in FeO_25000 and FeO_nopei [29]. Moreover, a further variation in the magnetization slope can be observed in the 250–300 K region for the FeO_25000 sample. Here, the combination of a shallow increase and a brisk settlement could be attributed to the Morin transition, which indicates the passage of hematite from a low-temperature antiferromagnetic to a high-temperature weakly ferromagnetic state. In fact, the low initial value of 250 K and the large spread up to 300 K is consistent with the formation of small-sized (<50 nm) hematite domains, which act as a secondary phase to the main one of magnetite [30]. Conversely, no such a trend can be observed in the FeO_nopei sample, where the disappearance of the Morin transition suggests the formation of hematite domains smaller than 20 nm [31].

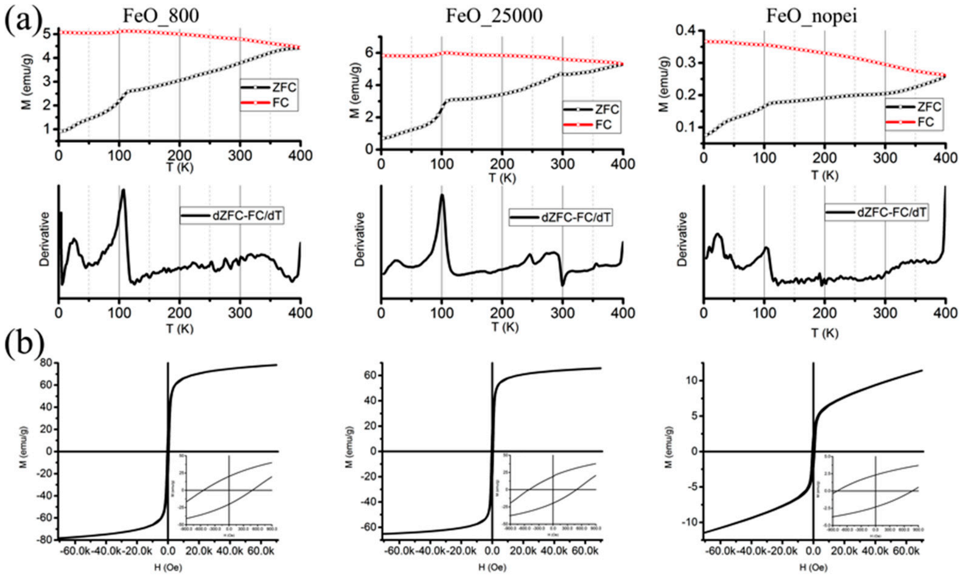

Figure 5. Zero-field-cooled and field-cooled (ZFC–FC) magnetization curves and derivative d(ZFC–FC)/dT curves (**a**) and hysteresis loops recorded at 4 K (**b**) for the FeO_800, FeO_25000, and FeO_nopei samples, respectively. The low-field regions of the hysteresis loops are reported as insets.

Moreover, two distinct trends emerge from the analysis of hysteresis loops recorded at 4 K and point out the effects of reduction on our systems, as displayed Figure 5b and summarized in Table 1.

Table 1. Magnetic parameters measured at 4 K from hysteresis loops of samples FeO_800, FeO_25000, and FeO_nopei, respectively. H_C: coercive field, M_{SAT}: saturation magnetization, M_R: remnant magnetization (remanence).

Sample	FeO_800	FeO_25000	FeO_nopei
H_C (Oe)	511	497	789
M_{SAT} (emu/g)	83	69	15
M_R (emu/g)	20	19	2

Only negligible variations can be observed when comparing the coercivity and remanence values (H_C and M_R) of FeO_800 and FeO_25000, which are both consistent with the formation of Fe_3O_4 NPs around 20 nm in size [32], while the FeO_nopei sample presents dramatically different values, with a strongly enhanced coercivity and a very low remanence that indicate a non-negligible presence of small-sized hematite domains [33,34]. The saturation magnetization M_{SAT}, on the other hand, shows a linear trend from FeO_800 to the FeO_25000 and FeO_nopei samples, with M_{SAT} values of 83 emu/g, 66 emu/g, and 11 emu/g, respectively. While the saturation value of the FeO_800 is lower, but still comparable to the bulk saturation value of 92 emu/g [35], the decrease observed in M_{SAT} for the remaining samples can be at first attributed to the presence of the antiferromagnetic hematite phase, which causes a depression of the magnetization values normalized by mass. This effect can be already observed in the FeO_25000 sample, but becomes dramatic in the FeO_nopei sample.

4. Discussion

The overall structural transformation process from the $FeCl_3$ iron precursor to iron oxide nanostructures previously described by Mohapatra [25] is composed of two different stages, namely the preparation of β-FeOOH NRs and their conversion to iron oxide nanostructures. In the first step, the hydrolysis of $FeCl_3{\cdot}6H_2O$ in aqueous media produced the synthesis of β-FeOOH NRs with different lengths and diameters depending on the presence of PEI as a capping agent.

To examine the role and influence of the PEI in the formation of β-FeOOH NRs, we just modified the "PEI conditions", while keeping constant the rest of the reaction conditions. Firstly, we tested the preparation of β-FeOOH NRs in absence of PEI, then we studied and compared the synthesis of nanorods in presence of two different branched PEIs, one with low molecular weight (800 g/mol), and the other one with a high molecular weight (25,000 g/mol). In the absence of PEI, β-FeOOH NPs were synthesized in a spindle-shaped morphology with an average length of 291 nm, as previously reported in the work of Mohapatra. The addition of PEI determined the synthesis of shorter nanorods; in particular, the length of the nanorods changed from 31.7 nm to 38.7 nm depending on the molecular weight of the polymer used in the synthesis (800 g/mol and 25,000 g/mol, respectively), while their diameter was kept constant in both samples. This proves that not only the presence or absence of PEI introduced during the reaction plays an important role in determining the aspect ratio of the β-FeOOH NRs, but also that the type of PEI determines changes in the length of the resulting NRs.

The second synthetical step requires a reduction of as-prepared NRs in OLA at 200 °C for 4 h. Here, the variations in the final synthetic products being dependent on PEI are even clearer. While the final FeO_nopei sample nearly maintains the original shape and size, albeit with a decrease in length with respect to the starting FeOOH_nopei sample, no size or shape retention is observed after the reduction of the FeOOH_800 and FeOOH_25000 samples, which evolve to polydisperse ensembles without dominant shapes or sizes. Furthermore, a structural characterization conducted by XRD, TEM, and HRTEM showed the complete conversion of β-FeOOH phase into iron oxide in the three samples, but it also highlighted the formation of a secondary phase, which depended on the synthetical route followed in the first step. In fact, the sole magnetite phase was observed in case of the low Mw_PEI sample (FeO_800), while a secondary hematite phase was observed in the other cases (FeO_25000 and FeO_nopei). While the magnetic separation operated by Mohapatra clearly explains the absence of hematite in their samples, its presence could offer hindsight on the mechanism of the reduction process. The most likely hypothesis is that in the first step of the reduction, β-FeOOH is converted into hematite, due to its having the highest stability among iron oxide phases [22,36]. Later, hematite changes into magnetite by a reduction process, therefore, the magnetite nanostructures could be synthesized through a two-step phase transformation: $\beta\text{-FeOOH} \rightarrow \alpha\text{-}Fe_2O_3 \rightarrow Fe_3O_4$, with hematite as an intermediate step [22]. Taking into account the differences in size observed in the as-prepared NRs used as starting material, the complete conversion from FeOOH to magnetite would require different amounts of time, depending on the size of the NPs. Thus, since the same reduction time was used for all the samples, shorter starting NRs are completely reduced to magnetite (FeO_800), while bigger NRs still present hematite as a secondary phase due to an incomplete reduction.

The results obtained by the magnetic characterization offer a further useful insight in the phase transition matter. In fact, it was already emphasized how the observation of the Verwey and Morin transitions in the ZFC–FC curves indicates the formation of the magnetite and hematite phases, respectively. However, a closer look at the magnetic features of each transition also offers some further structural information. In particular, the variation of the Verwey transition temperature observed between FEO_800 (T_V = 115 K) and FeO_25000 and FeO_nopei (T_V = 110 K) indicates that in the latter cases, the newly formed magnetite is likely structurally defective. Moreover, the proportional reduction observed in saturation magnetization with the increase in size of the starting NRs and the hematite-like coercive values observed in the hysteresis loop of FeO_nopei all prove the presence of a scale factor that affects the reduction of the NRs, with a complete reduction for the smaller FeO_800, a partial reduction for the intermediate FeO_25000, and a starting reduction for the big FeO_nopei sample.

Even taking aside all these factors, the major difference between our results and those shown by Mohapatra [25] lies in the different products obtained, despite applying an apparently similar approach to prepare magnetite rods. In fact, while our results are consistent with those of Mohapatra concerning the reduction of β-FeOOH NRs in absence of a capping ligand, the direct conversion of β-FeOOH NRs into magnetite NRs using OLA as a reducing agent, solvent, and capping ligand does not lead to magnetite NRs that keep their structural rodlike morphology. In fact, our results report that using similar mild reduction conditions leads to the collapse of the nanorod framework and to the subsequent formation of differently shaped NPs. Considering that an increase in porous and crystal defects is expected during the reduction processes due to the loss of H_2O [16,22], it could be hypothesized that this behavior is an effect of the poorer crystallinity of our as-prepared β-FeOOH NRs compared to the 30–70 nm NRs prepared by Mohapatra, as also suggested by the similarities in terms of crystallinity between our starting materials and their shortest nanorods (length = 25 nm), which also cannot retain the rod structure after the reduction step. A similar phenomenon was also observed when the reduction of the β-FeOOH NRs was carried out in strong reduction conditions, (e.g., using hydrazine at high concentration [19]). Then, the formation of magnetite NRs depends on the condition that the reduction-related defects are not enough to collapse the NR structure. The evidence of our results, obtained by two PEIs with different molecular weight (M_w = 800 g/mol and 25,000 g/mol) as capping ligands, suggests that the low crystallinity of short NRs cannot be simply overcome by changing PEIs. Conversely, there seems to be a PEI-dependent scale factor in the synthesis of β-FeOOH NRs, which is the key to the formation of NRs with minimum structural defects in the 30–70 nm length range.

5. Materials and Methods

5.1. Synthesis of the Materials: General Notes

Oleylamine (OLA, 70%), the iron precursor $FeCl_3 \cdot 6H_2O$ (98%), PEI (M_w = 800 g/mol) and PEI (M_w = 25,000 g/mol) were purchased from Sigma-Aldrich. (Darmstadt, Germany). Organic solvents like acetone and hexane were of analytical grade and obtained from various sources. All chemicals were used as received without any further purification. Some of the experiments were carried out using standard airless techniques: a vacuum/dry nitrogen gas Schlenk line was used for synthesis of Fe_3O_4 nanoparticles.

5.2. XRD Analysis

X-ray powder diffraction (XRD) was performed at room temperature using a Bruker D8 Advance system, equipped with a monochromatic copper radiation source Cu Kα = 0.154056 nm in the 20°–70° range with a scan step of 0.5°/min.

5.3. TEM HRTEM Imaging and Size Analysis

TEM imaging of all the samples was performed by an FEI Tecnai Spirit microscope, equipped with a lanthanum hexaboride thermionic electron source, a Twin objective lens, a Orius CCD camera (Gatan, Pleasanton, CA, USA), and operating at an acceleration voltage of 120 kV. HRTEM imaging was performed by an FEI Titan microscope, equipped with an X-FEG Schottky electron source, a SuperTwin objective lens, a Gatan 2k × 2k CCD camera, and operating at an acceleration voltage of 300 kV. Size analysis was performed on all the samples by considering 150 nanoparticles.

5.4. Magnetic Behavior Investigation

Magnetic characterization was performed on a MPMS SQUID magnetometer (Quantum Design, San Diego, CA, USA), equipped with a superconducting magnet producing fields up to 70 kOe and a Helium Quantum Design EverCool liquefier. Zero-field-cooled (ZFC) and field-cooled (FC) magnetizations were collected in the range of temperatures 4–400 K. ZFC curves were measured by cooling samples in a zero-magnetic-field and by subsequent increase of the temperature under an applied field of 50 Oe. FC curves were recorded by cooling the samples while maintaining the same applied field of 50 Oe. Hysteresis loops were recorded up to ±70 kOe at 4.0 K. M_{SAT} was determined by extrapolation of M values vs. $1/H$ for $1/H \rightarrow 0$. To prepare the samples, the solutions were dried and the resulting compounds were measured by thermogravimetric analysis (TGA) to assess the percentage of magnetic phase effectively formed. The dried compounds were subsequently redispersed in hexane in order to obtain new solutions with a fixed, common percentage of magnetic phases with respect to the hexane volume. Finally, fixed volumes of the new solutions were drop-casted on Teflon tape and left to dry in ambient conditions.

6. Conclusions

In our work, we have studied the effect of the capping agent PEI in the synthesis of the β-FeOOH NRs. Our results indicated that PEI plays an important role in the synthesis of β-FeOOH NRs with different sizes. In fact, when studying the reduction process from β-FeOOH NRs to Fe_3O_4 nanostructures of bigger-sized NPs prepared without PEI, original shape and size were generally maintained after reduction, while the introduction of two different PEIs determined significant variations in the shape and size of the starting NRs and of the final products, namely shorter and irregularly-shaped NPs. Thus, while the capping agent does not seem to improve the stability of shorter β-FeOOH NRs, its role is capital for the successful formation of longer NRs, since the choice of apparently similar capping agents can lead to dramatically different results.

Acknowledgments: The authors acknowledge financial support from the KAUST start-up and baseline funding of Andrea Falqui.

Author Contributions: Andrea Falqui conceived the experiments, analyzed the data and wrote the paper; Sergio Lentijo Mozo, Efisio Zuddas and Alberto Casu performed the experiments, analyzed the data and wrote the paper. All the authors discussed in-depth the paper.

Conflicts of Interest: The authors declare no conflict of interest.

References

1. Rossi, L.M.; Costa, N.J.S.; Silva, F.P.; Wojcieszak, R. Magnetic nanomaterials in catalysis: Advanced catalysts for magnetic separation and beyond. *Green Chem.* **2014**, *16*, 2906. [CrossRef]
2. Frey, N.A.; Peng, S.; Cheng, K.; Sun, S. Magnetic nanoparticles: Synthesis, functionalization, and applications in bioimaging and magnetic energy storage. *Chem. Soc. Rev.* **2009**, *38*, 2532–2542. [CrossRef] [PubMed]
3. Yoon, T.J.; Lee, H.; Shao, H.; Weissleder, R. Highly magnetic core–shell nanoparticles with a unique magnetization mechanism. *Angew. Chem. Int. Ed.* **2011**, *50*, 4663–4666. [CrossRef] [PubMed]

4. Chen, S.; Li, Y.; Guo, C.; Wang, J.; Ma, J.; Liang, X.; Yang, L.R.; Liu, H.Z. Temperature-responsive magnetite/PEO–PPO–PEO block copolymer nanoparticles for controlled drug targeting delivery. *Langmuir* **2007**, *23*, 12669–12676. [CrossRef] [PubMed]
5. Laurent, S.; Dutz, S.; Hafeli, U.O.; Mahmoudi, M. Magnetic fluid hyperthermia: Focus on superparamagnetic iron oxide nanoparticles. *Adv. Colloid Interface Sci.* **2011**, *166*, 8–23. [CrossRef] [PubMed]
6. Suh, S.K.; Yuet, K.; Hwang, D.K.; Bong, K.W.; Doyle, P.S.; Hatton, T.A. Synthesis of nonspherical superparamagnetic particles: In situ coprecipitation of magnetic nanoparticles in microgels prepared by stop-flow lithography. *J. Am. Chem. Soc.* **2012**, *134*, 7337–7343. [CrossRef] [PubMed]
7. Tian, Y.; Yu, B.; Li, X.; Li, K. Facile solvothermal synthesis of monodisperse Fe_3O_4 nanocrystals with precise size control of one nanometre as potential MRI contrast agents. *J. Mater. Chem.* **2011**, *21*, 2476–2481. [CrossRef]
8. Lemine, O.M.; Omri, K.; Zhang, B.; El Mir, L.; Sajieddine, M.; Alyamani, A.; Bououdina, M. Sol–gel synthesis of 8 nm magnetite (Fe_3O_4) nanoparticles and their magnetic properties. *Superlattices Microstruct.* **2012**, *52*, 793–799. [CrossRef]
9. Park, J.; An, K.; Hwang, Y.; Park, J.G.; Noh, H.J.; Kim, K.Y.; Park, J.H.; Hwang, N.M.; Hyeon, T. Ultra-large-scale syntheses of monodisperse nanocrystals. *Nat. Mater.* **2004**, *3*, 891–895. [CrossRef] [PubMed]
10. Zhou, Z.; Zhu, X.; Wu, D.; Chen, Q.; Huang, D.; Sun, C.; Xin, J.; Ni, K.; Gao, J. Anisotropic shaped iron oxide nanostructures: Controlled synthesis and proton relaxation shortening effects. *Chem. Mater.* **2015**, *27*, 3505–3515. [CrossRef]
11. Muraliganth, T.; Murugan, A.V.; Manthiram, A. Facile synthesis of carbon-decorated single-crystalline Fe_3O_4 nanowires and their application as high performance anode in lithium ion batteries. *Chem. Commun.* **2009**, 7360–7362. [CrossRef] [PubMed]
12. Bao, L.; Low, W.-L.; Jiang, J.; Ying, J.Y. Colloidal synthesis of magnetic nanorods with tuneable aspect ratios. *J. Mater. Chem.* **2012**, *22*, 7117–7120. [CrossRef]
13. Si, J.-C.; Xing, Y.; Peng, M.-L.; Zhang, C.; Buske, N.; Chen, C.; Cui, Y.-L. Solvothermal synthesis of tunable iron oxide nanorods and their transfer from organic phase to water phase. *Cryst. Eng. Commun.* **2014**, *16*, 512–516. [CrossRef]
14. Tadic, M.; Milosevic, I.; Kralj, S.; Saboungi, M.-L.; Motte, L. Ferromagnetic behavior and exchange bias effect in akaganeite nanorods. *Appl. Phys. Lett.* **2015**, *106*, 183706. [CrossRef]
15. Guo, H.; Barnard, A.S. Naturally occurring iron oxide nanoparticles: Morphology, surface chemistry and environmental stability. *J. Mat. Chem. A* **2013**, *1*, 27–42. [CrossRef]
16. Chaudhari, N.K.; Yu, J.-S. Size control synthesis of uniform β-FeOOH to high coercive field porous magnetic. *J. Phys. Chem. C* **2008**, *112*, 19957–19962. [CrossRef]
17. Chen, M.; Tang, B.; Nikles, D.E. Preparation of iron nanoparticles by reduction of acicular β-FeOOH particles. *IEEE Trans. Magn.* **1998**, *34*, 1141–1143. [CrossRef]
18. Peng, Z.; Wu, M.; Xiong, Y.; Wang, J.; Chen, Q. Synthesis of magnetite nanorods through reduction of β-FeOOH. *Chem. Lett.* **2005**, *34*, 636–637. [CrossRef]
19. Yue, J.; Jiang, X.; Yu, A. Experimental and theoretical study on the β-FeOOH nanorods: Growth and conversion. *J. Nanopart. Res.* **2011**, *13*, 3961–3974. [CrossRef]
20. Milosevic, I.; Jouni, H.; David, C.; Warmont, F.; Bonnin, D.; Motte, L. Facile microwave process in water for the fabrication of magnetic nanorods. *J. Phys. Chem. C* **2011**, *115*, 18999–19004. [CrossRef]
21. Chen, S.; Feng, J.; Guo, X.; Hong, J.; Ding, W. One-step wet chemistry for preparation of magnetite nanorods. *Mater. Lett.* **2005**, *59*, 985–988. [CrossRef]
22. Piao, Y.; Kim, J.; Na, H.B.; Kim, D.; Baek, J.S.; Ko, M.K.; Lee, J.H.; Shokouhimehr, M.; Hieon, T. Wrap–bake–peel process for nanostructural transformation from β-FeOOH nanorods to biocompatible iron oxide nanocapsules. *Nat. Mater.* **2008**, *7*, 242–247. [CrossRef] [PubMed]
23. Bomati-Miguel, O.; Rebolledo, A.F.; Tartaj, P. Controlled formation of porous magnetic nanorods via a liquid/liquid solvothermal method. *Chem. Commun.* **2008**, 4168–4170. [CrossRef] [PubMed]
24. Choi, J.; Cha, J.; Lee, J.K. Synthesis of various magnetite nanoparticles through simple phase transformation and their shape-dependent magnetic properties. *RSC Adv.* **2013**, *3*, 8365–8371. [CrossRef]
25. Mohapatra, J.; Mitra, A.; Tyagi, H.; Bahadur, D.; Aslam, M. Iron oxide nanorods as high-performance magnetic resonance imaging contrast agents. *Nanoscale* **2015**, *7*, 9174–9184. [CrossRef] [PubMed]

26. Moon, J.-M.; Wei, A. Uniform gold nanorod from polyethylenimine-coated alumina templates. *J. Phys. Chem. B* **2005**, *109*, 23336–23341. [CrossRef] [PubMed]
27. Chen, L.-Y.; Yin, Y.-T.; Chen, C.-H.; Chiou, J.-W. Influence of polyethyleneimine and ammonium on the growth of ZnO nanowires by hydrothermal method. *J. Phys. Chem. C* **2011**, *115*, 20913–20919. [CrossRef]
28. Prozorov, R.; Prozorov, T.; Mallapragada, S.K.; Narasimhan, B.; Williams, T.J.; Bazylinski, D.A. Magnetic irreversibility and the Verwey transition in nanocrystalline bacterial magnetite. *Phys. Rev. B* **2007**, *76*, 054406. [CrossRef]
29. Yang, J.B.; Zhou, X.D.; Yelon, W.B.; James, W.J.; Cai, Q.; Gopalakrishnan, K.V.; Malik, S.K.; Sun, X.C.; Nikles, D.E. Magnetic and structural studies of the Verwey transition in $Fe_{3-\delta}O_4$ nanoparticles. *J. Appl. Phys.* **2004**, *95*, 7540. [CrossRef]
30. Bhowmik, R.N.; Saravanan, A. Surface magnetism, Morin transition, and magnetic dynamics in antiferromagnetic α-Fe_2O_3 (hematite) nanograins. *J. Appl. Phys.* **2010**, *107*, 053916. [CrossRef]
31. Wu, C.; Yin, P.; Zhu, X.; OuYang, C.; Xie, Y. Synthesis of hematite (α-Fe_2O_3) nanorods: Diameter-size and shape effects on their applications in magnetism, lithium ion battery, and gas sensors. *J. Phys. Chem. B* **2006**, *110*, 17806–17812. [CrossRef] [PubMed]
32. Guardia, P.; Pérez, N.; Labarta, A.; Batlle, X. Controlled synthesis of iron oxide nanoparticles over a wide size range. *Langmuir* **2010**, *26*, 5843–5847. [CrossRef] [PubMed]
33. André-Filho, J.; León-Félix, L.; Coaquira, J.A.H.; Garg, V.K.; Oliveira, A.C. Size dependence of the magnetic and hyperfine properties of nanostructured hematite (α-Fe_2O_3) powders prepared by the ball milling technique. In Proceedings of the 13th Latin American Conference on the Applications of the Mössbauer Effect (LACAME 2012), Medellin, Colombia, 11–16 November 2012.
34. Zhao, Y.; Dunnill, C.W.; Zhu, Y.; Gregory, D.H.; Kockenberger, W.; Li, Y.; Hu, W.; Ahmad, I.; McCartney, D.G. Low-temperature magnetic properties of hematite nanorods. *Chem. Mater.* **2007**, *19*, 916–921. [CrossRef]
35. Mikhaylova, M.; Kim, D.Y.; Bobrysheva, N.; Osmolowsky, M.; Semenov, V.; Tsakalakos, T.; Muhammed, M. Superparamagnetism of magnetite nanoparticles: Dependence on surface modification. *Langmuir* **2004**, *20*, 2472–2477. [CrossRef] [PubMed]
36. Wu, W.; Wu, Z.; Yu, T.; Jiang, C.; Kim, W.-S. Recent progress on magnetic iron oxide nanoparticles: Synthesis, surface functional strategies and biomedical applications. *Sci. Technol. Adv. Mater.* **2015**, *16*, 023501. [CrossRef] [PubMed]